



Self-assembly of stacked layers of Mn_3O_4 nanosheets using a scalable chemical strategy for enhanced, flexible, electrochemical energy storage

Deepak P. Dubal*, Rudolf Holze

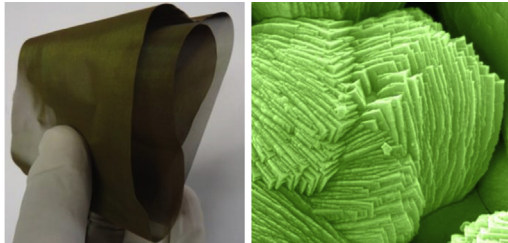
Technische Universität Chemnitz, Institut für Chemie, AG Elektrochemie, D-09107 Chemnitz, Germany



HIGHLIGHTS

- Simple and scalable strategy for the growth of Mn_3O_4 stacked nanosheets.
- Stacked nanosheet-like nanostructure with high surface area.
- Mn_3O_4 stacked nanosheets provide high specific capacitance and stability.
- Mn_3O_4 stacked nanosheets provide high energy and power density values.

GRAPHICAL ABSTRACT



Self-assembly of stacked layers of Mn_3O_4 nanosheets for highly flexible supercapacitor application

ARTICLE INFO

Article history:

Received 23 November 2012

Received in revised form

14 January 2013

Accepted 17 January 2013

Available online 29 March 2013

Keywords:

Stacked nanosheets

Chemical bath deposition

Supercapacitors

Ragone plot

ABSTRACT

Uniformly stacked nanosheets of Mn_3O_4 with different sizes and crystallinities have been self-assembled on a titanium substrate by a simple and scalable strategy. When the prepared Mn_3O_4 nanosheets are applied as electrode materials for supercapacitors, they exhibit enhanced electrochemical performances due to the high utilization of active materials. More significantly, based on these stacked nanostructures, we have discussed the relationships between specific area, crystallinity and the electrochemical performance of this material. The stacked nanostructures exhibit a high specific capacitance of 398 F g^{-1} at a scan rate of 0.005 V s^{-1} over a potential window from -0.1 to 0.9 V with high rate capability and good cycling stability. These results demonstrate the importance of a well-arranged and stacked architecture of Mn_3O_4 in high-energy-storage applications.

© 2013 Elsevier B.V. All rights reserved.

1. Introduction

Nanostructured materials have been the focal point of much research due to their unique mechanical, electrical and optical properties [1–3]. However, control over the size, structure and composition of nanostructured materials is still the most essential challenge for the fundamental understanding and practical application of nanostructured materials [4,5]. Recently, the most essential issue in

our society is development of new energy storage devices with alternative energy sources. Nanostructured materials are promising for electrochemical supercapacitor applications and for the development of new energy-storage devices [6,7]. Among different energy-storage devices, supercapacitors are the most prominent type of device because they can provide higher energy density than conventional capacitors and higher power density than batteries, which is encouraging for next-generation energy storage devices [8,9].

Manganese oxide is one of the most durable and powerful candidates for the supercapacitor electrode material due to its low cost, non-toxicity, environmentally friendly nature and high specific capacitance [10,11]. Manganese oxide requires a neutral aqueous

* Corresponding author. Tel.: +49 371 531 982874; fax: +49 371 531 21269.

E-mail addresses: dubaldeepak2@gmail.com (D.P. Dubal), rudolf.holze@chemie.tu-chemnitz.de (R. Holze).

electrolyte, such as Na_2SO_4 or K_2SO_4 , as a “green electrolyte” in the supercapacitor [12,13]. Among different manganese oxide polymorphs, Mn_3O_4 has been the subject of relatively little research compared with MnO_2 and MnO . However, it plays important roles in energy storage, catalysts, and soft magnetic materials, among others, and has recently drawn increased attention [14,15]. As far as we know, only a few reports have been related to the electrochemical capacitive properties of Mn_3O_4 . To develop high-performance electrode materials, the activity of electro-active species and the transport of electrons, electrolytes and reactants must be considered simultaneously [16,17]. The activity of the electrode material is mainly dependent on the microstructure of the active material. In the field of materials science, the fabrication of a well-defined morphology with tunable size, macro/mesopores and nanoarchitecture of the nanostructured materials are considered to be essential from the scientific as well as the technological point of view [18,19].

Different synthesis methods such as solid-state reaction, γ -ray irradiation, and chemical bath deposition (CBD) are used to develop different morphologies of Mn_3O_4 , such as nanorods/nanowires, mesoporous/hollow spheres, nanofibers, etc. [20,21]. In particular, the chemical bath deposition (CBD) method, as a typical solution-based approach, has proven to be effective and convenient in preparing various inorganic materials with diverse, controllable morphologies and architectures [22]. The advantages of this method include easily controllable reaction conditions, relatively large scale and high yield in terms of the quantity of desired products, and frequently using water or another solvent as the reaction medium.

Herein, a mild, simple, and scalable strategy has been developed to realize the synthesis of self-assembled, stacked layers of Mn_3O_4 nanosheets. The size and crystalline nature of the stacked nanosheet layers can be easily tuned by changing the concentration of the complexing agent. More significantly, the relationships of these factors with the electrochemical performances have been investigated. Among them, the samples synthesized at low concentration which have an especially high specific area ($104 \text{ m}^2 \text{ g}^{-1}$), uniform pore size distribution and poor crystallinity, demonstrate the highest specific capacitance with a high rate and cycling stability. Thus, the results indicate the importance of morphologies (size and crystalline nature) in the fabrication of a high-performance supercapacitive electrode material.

2. Experimental details

Synthesis of stacked nanosheets of Mn_3O_4 thin films is based on a CBD method by immersing the substrates into an aqueous solution of manganese sulfate complexed with hexamethylenetetramine (HMT). Firstly, solution mixtures of 0.1 M manganese sulfate with three different concentrations of HMT (0.05, 0.1 and 0.15 M) were prepared. Well cleaned titanium substrates were immersed in the above-prepared baths at temperature of 343 K. During precipitation, a heterogeneous reaction occurred and the Mn_3O_4 was deposited on the substrates. The deposition time for Mn_3O_4 sample at 343 K kept constant 3 h for all the three baths (Supporting information S1). The films were annealed at 473 K for 2 h, in order to remove hydroxide and to improve the crystallinity of the deposited films. The films obtained after the deposition period of 3 h, for the HMT concentration of 0.05, 0.1 and 0.15 M, are hereafter denoted as M1, M2 and M3, respectively.

Structural identification of Mn_3O_4 films was carried out using Rigaku Rotaflex RU-200B diffractometer using a $\text{Cu K}\alpha$ ($\lambda = 1.5418 \text{ \AA}$) source with a Ni filter at 40 kV and 40 mA at a scan rate of 0.02 s^{-1} . The microstructures of films were examined with a field emission scanning electron microscope (FESEM JEOL JSM-7500F). TEM and HRTEM observations were conducted using JEOL JEM-2100 operated at 200 kV. X-ray photoelectron spectroscopy (XPS) was performed with

a VG Multilab 2000 from Thermo VG Scientific UK. N_2 adsorption/desorption was determined by Brunauer–Emmett–Teller (BET) measurements using an ASAP-2010 surface area analyzer. Cyclic voltammograms (CVs) were performed with AMETEK Solartron analytical system model 1400 and an electrochemical cell consisted of Mn_3O_4 stacked nanosheets as the working electrode, and Ag/AgCl and platinum were used as the reference and counter electrodes in 1 M Na_2SO_4 . Electrochemical impedance spectroscopy (EIS) measurements of stacked Mn_3O_4 nanosheets were carried out using the multi-impedance test system in the frequency range from 10 kHz to 10 mHz with an AC amplitude of 10 mV.

3. Results and discussion

3.1. Film formation and reaction mechanism

In CBD method, when the ionic product of anion and cation exceeds the solubility product then the solution becomes supersaturated and hence precipitation occurs and ions combine on the substrate and in the solution to form nuclei. Film growth can take place by two different ways: (1) via ion-by-ion condensation of materials and (2) by the adsorption of colloidal particles from the solution on the substrate. Solid phase formation from the solution includes two steps of nucleation and particle growth. Nucleation implies that the clusters of molecules formed undergo rapid decomposition and particles combine to grow in thin film form. Normally, metal ions are complexed, hence reaction takes place between slowly released metal ions to form a product in thin film. Mn_3O_4 thin film depositions take place on titanium substrates via slow hydrolysis of manganese in the sulfate solution. This can be represented as follows. Here, it is thought that HMT serves as a source of a weak reducing agent. Formaldehyde and ammonia are produced by the hydrolysis of HMT at an elevated temperature [23]. The low reaction temperature and unstirred chemical bath slowly releases free Mn^{2+} cations from the stable precursor. These Mn^{2+} cations form ammine complexes of $\text{Mn}(\text{NH}_3)_n^{2+}$ ($n = 1\text{--}4$) with NH_3 (aq) in moderately basic media ($\text{pH} \sim 8$). The reaction is as follows:

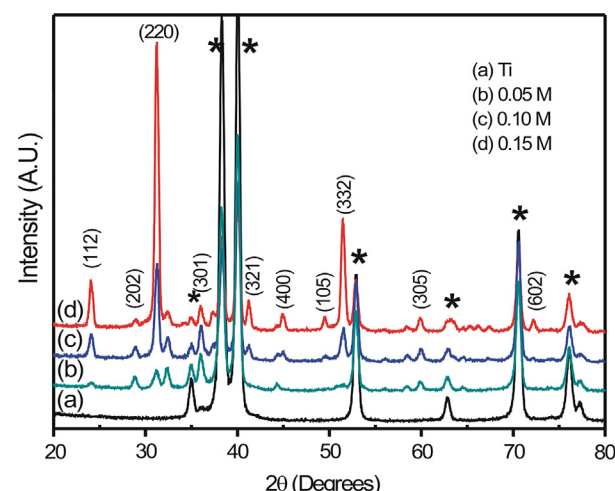
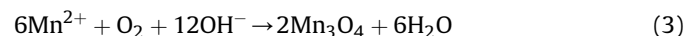
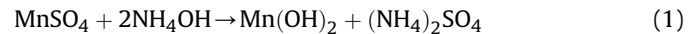


Fig. 1. XRD patterns of Mn_3O_4 samples at three different concentrations of HMT on titanium substrate.

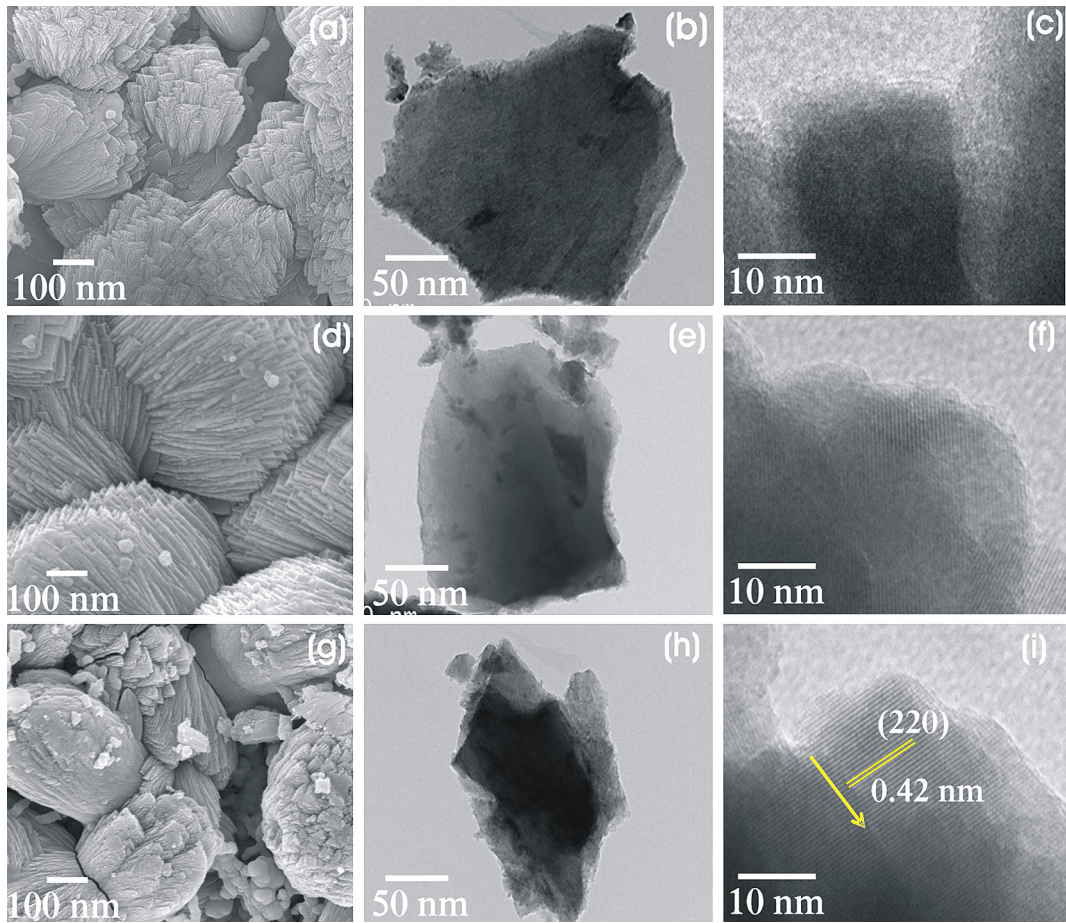


Fig. 2. SEM, TEM and HRTEM of (a–c) sample M1 (d–f) sample M2 and (g–i) sample M3 on titanium substrate, respectively.

Coordination compound of manganese ammonium complex might play a role in controlling not only release velocity of Mn^{2+} ions, but also growth direction of Mn_3O_4 nanocrystal. Recently, the effects of pH and ammonia on the Mn_3O_4 morphology were investigated [24,25]. Here excess NH_3 acts as ligand, which gets adsorbed on two surfaces of nanoparticles, to reduce the growth rate of two planes. As a result, the NH_3 molecules covered edge of nanosheets grow very fast and stacked nanosheets are formed.

3.2. Structural studies

The X-ray diffraction study was carried out for the determination of crystal structure along with structural changes and identification of phases of prepared Mn_3O_4 thin films. Fig. 1 shows XRD patterns of polycrystalline Mn_3O_4 stacked nanosheets prepared at different HMT concentrations (M1, M2 and M3) on titanium substrate. The planes corresponding to (112), (202), (220), (301), (321), (400), (105), (332), (305) and (602) are in good agreement with the standard values of tetragonal hausmannite Mn_3O_4 structure. The calculated lattice constants of $a = 5.752 \text{ \AA}$, $b = 5.752 \text{ \AA}$ and $c = 9.45 \text{ \AA}$ are also in a good agreement with standard lattice constants from JCPDS card no. 01-75-1560. Also from Fig. 1, it is clearly seen that as the concentration of HMT increases the crystallinity of Mn_3O_4 structure is also increased. Thus XRD patterns showed that the stacked Mn_3O_4 nanosheets are phase-pure and well-crystalline. It is well known that hausmannite Mn_3O_4 is a normal spinel structure with tetragonal distortion elongated along the c -axis due to Jahn–Teller effect on the Mn^{3+} ion. Manganese

ions are located in the octahedral B-site (Mn^{3+}) and tetrahedral A-site (Mn^{2+}) corresponding to a normal spinel structure [26].

3.3. Surface morphological analysis

The corresponding morphologies and detailed structures were characterized by both FESEM and TEM analysis, as shown in Fig. 2. Fig. 2(a) shows the SEM image of the products synthesized at low HMT concentration (M1). The products look like dense stacked nanosheets assembled nearly perpendicular to the substrate. Most of the nanosheets are aggregated together (Supporting information S2). However, on the basis of the observations from the TEM images (Fig. 2(b, c)), the products seem to be constituted with thin nanosheets that are loosely collected each other. The TEM images also confirm the thin nanostructures of the products, which is in good agreement with SEM results. When the concentration of HMT was increased, uniform stacking of Mn_3O_4 nanosheets (M2) can be seen in Fig. 2(d). The SEM image suggests that the sample M2 possesses a relative better alignment of stacked nanosheets on the surface than the sample M1. From the TEM and high magnification TEM observations (Fig. 2(e, f)), it can be seen that the nanosheets are thicker and possess a relatively better crystalline nature on the surface than the sample M1. The stacked nanosheets in the sample M2 possess a larger size than that of sample M1 due to the increased HMT concentration. As the HMT concentration further increases, the stacked nanosheets grow further nearly perpendicular to surface with increased thickness (the sample M3, Fig. 2(g)). Fig. 2(h) shows the TEM image of a representative stacked nanosheet of Mn_3O_4

nanostructure, which is in good agreement with the results from the SEM image. A high magnification TEM image of the sample M3 shows highly crystalline structure than both M1 and M2, as shown in Fig. 2(i). The well-resolved lattice fringes give an interplanar spacing of 0.42 nm, which is in good agreement with the distance of the (220) plane. It is reasonable that the stacked nanosheets become larger with better crystallinity when the HMT concentration increases, hence resulting in thicker stacked nanostructures.

A possible growth process with corresponding schematic illustration is proposed in Fig. 3. Initially, the partial hydrolysis of HMT produces formaldehyde and ammonia [27]. Ammonia can form a complex with Mn^{2+} , which decreases the free Mn^{2+} ion concentration and reduces the rate of crystal growth. Formation of manganese ammonium complex avoids homogeneous nucleation in the solution due to the binding of Mn^{2+} ions and provides priority to heterogeneous nucleation on substrate. As the reaction time increases, hydrolysis of more HMT molecules takes place. This increases the concentration of OH^- in the solution which encourages the formation of thin Mn_3O_4 nanosheets [28]. Here, HMT provides controlled supply of ammonia via the hydrolysis reaction (1), while unreacted HMT selectively adsorbed on the Mn_3O_4 nanoparticles due to its high binding capacity [29], resulting in the formation of nanosheets. According to thermodynamics, the surface energy of an individual nanosheet is high, therefore, they aggregate perpendicularly to the surface planes in order to decrease the surface energy [30]. Therefore, as the reaction proceeds, the thin sheets would self-aggregate to form Mn_3O_4 stacked sheet-like nanostructures for minimizing the overall surface energy.

3.4. XPS and BET analysis

In order to investigate the oxidation state of Mn in Mn_3O_4 , the XPS analyses were performed (Supporting Information S3). Fig. 4A displays the XPS spectra of Mn_3O_4 thin films. The $Mn2P_{3/2}$ peak observed at 641.65 eV and the $Mn2P_{1/2}$ peak at 653.22 eV indicate that the Mn is in oxidation state of Mn^{2+} [31]. The difference between binding energy values of $Mn2P_{3/2}$ and $Mn2P_{1/2}$ levels comes from spin-orbit splitting. In present case, the observed spin-orbit splitting is 11.6 eV. Similar types of results are reported elsewhere [32]. The O1s spectrum of Mn_3O_4 was also analyzed by curve fitting (Fig. 4B). The spectrum is fitted with three components observed at 529.7, 531.2, and 532.5 eV which are related to Mn–O–Mn for the tetravalent oxide, Mn–OH for hydrated trivalent oxide and H–O–H

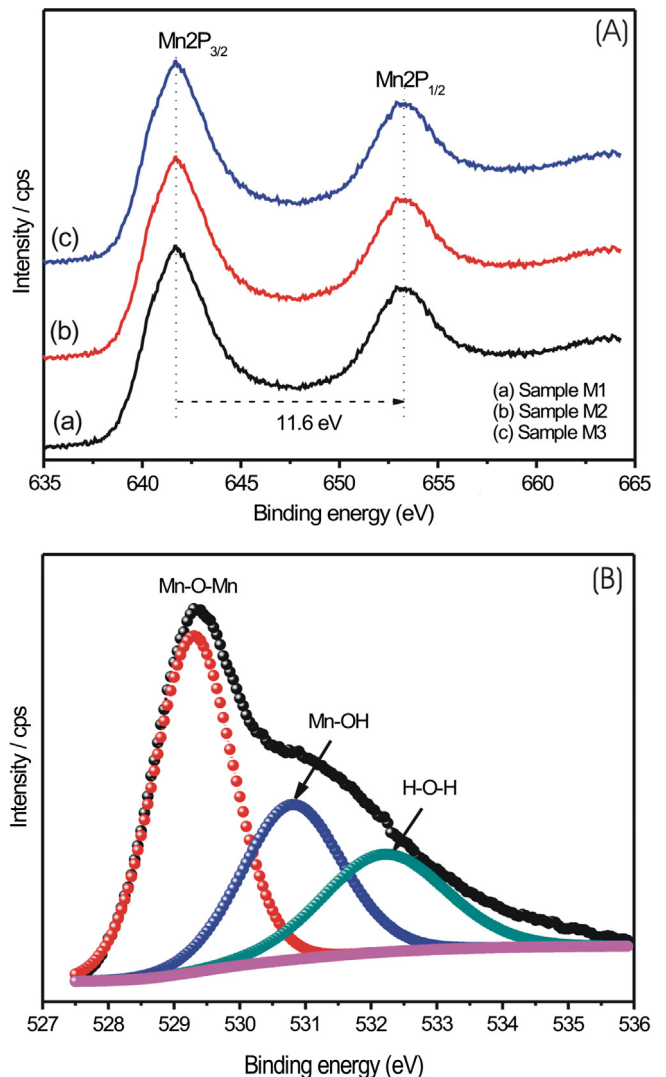


Fig. 4. (A) XPS spectra of Mn_3O_4 samples prepared at different HMT concentrations. (B) O1s spectrum of sample M1.



Fig. 3. Schematic depiction of the selective formation of Mn_3O_4 stacked nanosheets on the substrate.

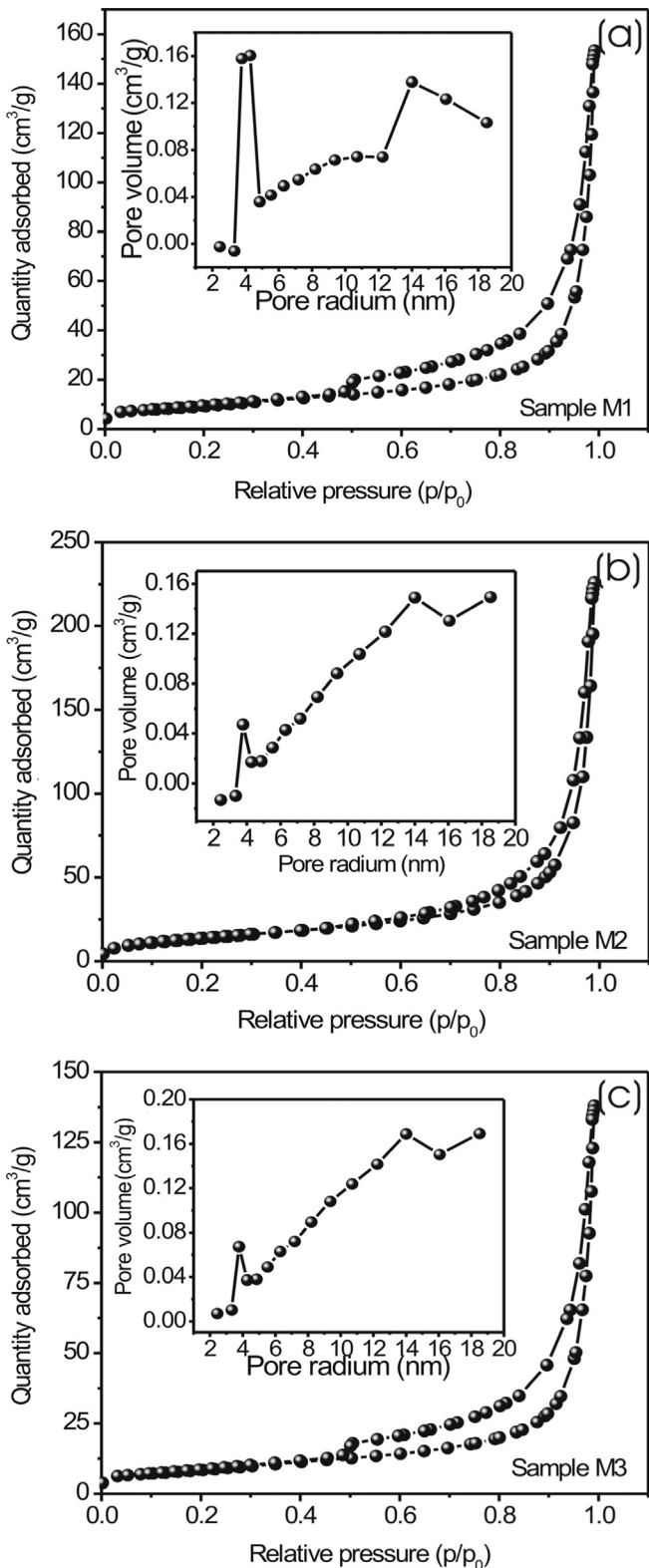


Fig. 5. (a–c) Nitrogen adsorption–desorption isotherms of sample M1, M2 and M3 with corresponding (inset) pore size distribution curves.

for residual water, respectively [33]. Fig. 5(a–c) shows the nitrogen adsorption and desorption isotherms and the corresponding pore size distributions (inset) of Mn_3O_4 samples. The specific surface areas were calculated from the Brunauer–Emmett–Teller (BET) method and the pore size distributions (PSD) were obtained by

means of the Barrett–Joyner–Halenda (BJH) equation using the adsorption isotherm branch. The BET specific surface areas of samples M1, M2 and M3 were found to be 104, 82 and $69 \text{ m}^2 \text{ g}^{-1}$, respectively. The pore size distribution curves of stacked Mn_3O_4 nanosheets are also shown in inset of Fig. 5. The most of the pores are observed in the range of 2–20 nm, with a centered pore distributions at around 3.97 nm, 3.94 nm and 3.92 nm for M1, M2 and M3 samples, respectively indicating that pores of stacked nanosheets are mainly mesopores with some micropores. It is also seen that the size of mesopores varies with increase in the size of nanosheets (as seen from peak intensity in BJH curves). This mesoporous structure of stacked Mn_3O_4 nanosheets could provide easy access for the ions in the electrolyte as well as short diffusion path for intercalation and deintercalation [34]. Further all the samples have characteristics bimodal pore size distribution. The bimodal porosity of samples is an amalgamation of internal space of the agglomerated nanosheets, surface porosity of the nanosheets and the porosity due to internal space of bunch of nanosheets. The pore size distribution of all Mn_3O_4 samples is slightly narrow which further supports the better homogeneity in the surface morphology and porosity of samples. In present investigation, we tuned the size and crystalline nature of Mn_3O_4 stacked nanosheets by adjusting the concentration of complexing agent which directly affects the surface area and shows a corresponding impact on the electrochemical properties.

3.5. Cyclic voltammetry

Cyclic voltammetry (CV) was employed to characterize the capacitive performances of the Mn_3O_4 stacked nanosheets, as shown in Fig. 6. The CV curves were recorded with the sample that was first stabilized by cycling 200 times. It can be clearly observed that the CV curves of all the three samples (Fig. 6A) show the similar rectangular shapes but with increased areas from the sample M1 to M3, which might be caused from the increased mass loadings of the samples (with increasing HMT concentration). Further, Fig. 6B shows the CV curves at different scan rates over the sample M1 and it is seen that there is no significant change in the rectangular shape with the increasing scan rates, indicating that the faraday redox reactions are electrochemically reversible [35]. At the scan rate of 0.005 V s^{-1} , the corresponding specific capacitances of Mn_3O_4 stacked nanosheets for the samples M1, M2 and M3 were 398 , 332 and 278 F g^{-1} for the mass loading of 0.023 g cm^{-2} , 0.027 g cm^{-2} and 0.029 g cm^{-2} , respectively. These results demonstrate that Mn_3O_4 stacked nanosheets are promising electrode materials for an electrochemical capacitor. The values reported here outperform as compared with other reports. Dai et al. [36] reported 133 F g^{-1} for spinel Mn_3O_4 layered nanoarchitectures with potential window of 0.9 V . Ahmed et al. [37] synthesized Mn_3O_4 hexagonal nanoplates and nanoparticles with specific capacitance of 237 F g^{-1} and 226 F g^{-1} , respectively with potential window of 0.8 V . In previous report [38], Mn_3O_4 thin films with triangular shaped nanoparticles showed specific capacitance of 284 F g^{-1} . In the present investigation, high specific capacitance and wide potential window (398 F g^{-1} with 1.0 V) may be attributed to the high surface area and vertically arranged stacked nanosheets-like architecture, which is beneficial for intercalation/deintercalation of Na^+ and H^+ ions. Fig. 6C shows the variation of specific capacitance with scan rate of all three samples (M1, M2 and M3). The specific capacitance decreases, as the scan rate is increased from 0.005 to 0.1 V s^{-1} . During the charging–discharging process in the stacked Mn_3O_4 , protons are exchanged with the electrolyte and electrode interface. Since this proton transfer rate is slow, high scan rate leads to either depletion or saturation of the protons during the charging/discharging process. This results in the

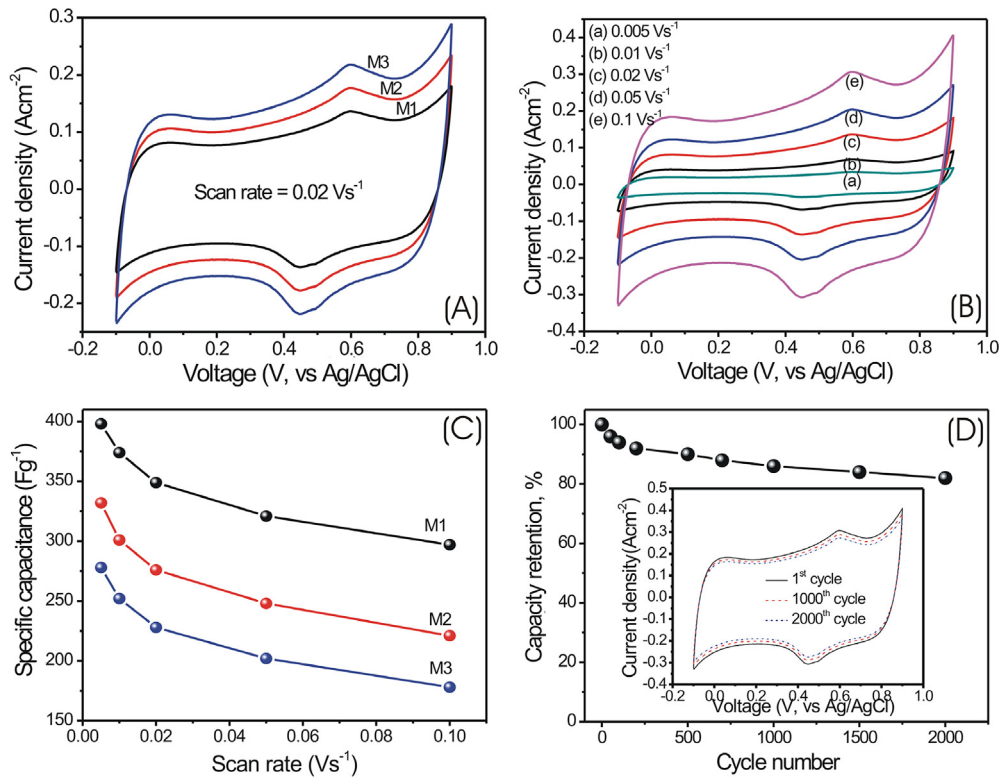


Fig. 6. (A) Typical cyclic voltammograms (CVs) of Mn_3O_4 samples (M1, M2 and M3) at 0.02 V s^{-1} scan rate, (B) CV curves of samples M1 at different scanning rates in 1 M Na_2SO_4 electrolyte, (C) variation of specific capacitance of Mn_3O_4 electrodes with scan rate, (D) variation of capacity retention with number of cycles. Inset shows cyclic voltammograms (CVs) of the sample M1 at 1st, 1000th and 2000th cycle.

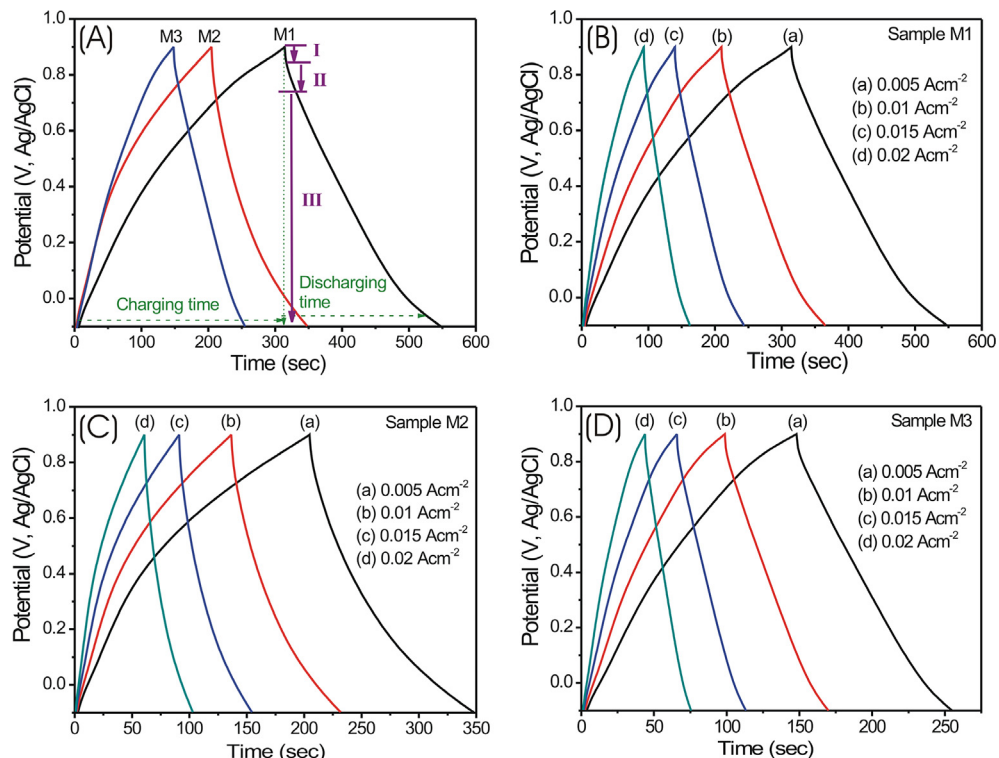


Fig. 7. (A) Galvanostatic charge–discharge curves of three Mn_3O_4 electrodes (M1, M2 and M3) at 0.005 A cm^{-2} current density. (B–D) Galvanostatic charge–discharge curves of Mn_3O_4 samples at different current densities.

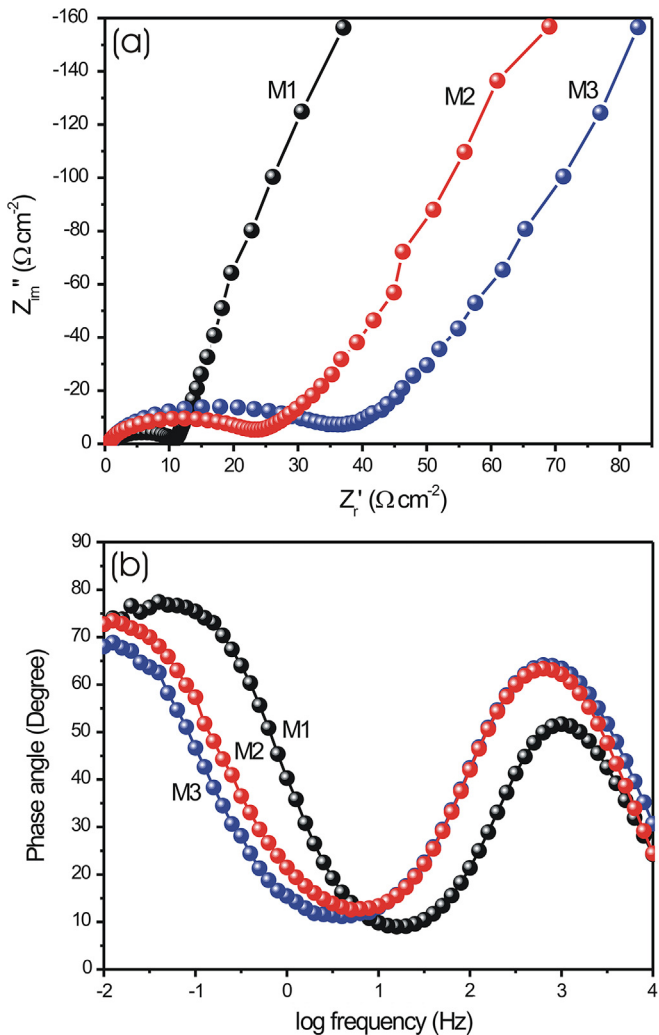


Fig. 8. (a) Nyquist plots and (b) Bode plots of Mn_3O_4 samples, respectively.

increase of ionic resistivity which reduces the capacitance of the Mn_3O_4 nanosheet electrode. The decrease in capacitance suggests that at high charging–discharging rates all the active species of the electrode are not able to take part in the charge storage process. Hence, the specific capacitance obtained at slow scan rate could be considered to the full utilization of electrode material [39]. The electrochemical stabilities were investigated by repeating the CV test of sample M1 at a scan rate of 0.1 V s^{-1} for 2000 cycles, and the good cycling stability results were shown in Fig. 6D. From the CVs (inset of Fig. 6D) it is seen that all the curves almost overlap each other, indicating a good cycling stability. It is interesting to note that the capacity retained after 2000 cycles is about 82% of the maximum specific capacitance as seen from Fig. 6D. These results demonstrate that the stacked Mn_3O_4 nanosheets are very stable in the repeated cycles as supercapacitor electrode material. Good cycle performance of the Mn_3O_4 nanosheets is attributed to its stacked nanoarchitecture, which provides high surface area with spaces for facilitated transport of charges and minimizes ion diffusion path.

Fig. 7A shows the charge–discharge curves of the stacked Mn_3O_4 nanosheet samples (M1, M2 and M3) obtained in 1 M Na_2SO_4 at current density of 0.005 A cm^{-2} . The charging and discharging curves are not symmetric. The curve shows three different regimes as follows: in regime I, at the starting of discharge there is sudden drop in the voltage which corresponds to the internal

Table 1

Value of power for the heat production at the internal resistance and loss factors of Mn_3O_4 stacked nanosheets in the lower and higher frequency region.

Sample	Phase angle (°)	Power corresponds to heat production (%)	Loss factor
M1	77.02	22	0.23
	51.50	62	0.79
M2	73.20	29	0.31
	63.26	44	0.50
M3	68.44	36	0.39
	64.38	42	0.47

resistance of the electrode material. In regime II, there is linear variation of potential with time, which indicates double layer capacitance caused due to the charge separation at electrode/electrolyte interface. Finally, there is slope variation of potential with time (regime III), indicating pseudo-capacitive behavior, resulted from redox reaction between electrolyte and Mn_3O_4 electrode [40]. Fig. 7(B–D) shows the galvanostatic charge–discharge curves of all the three Mn_3O_4 electrodes at different current densities. The shape of the discharge curves shows the characteristics of pseudo-capacitance, which is in agreement with the result of the CV a curve. As discharge current increases, the voltage (IR) drop increases and capacitance decreases. The specific capacitance (C) can be calculated as follows:

$$C = \frac{I \times \Delta t}{\Delta V \times m} \quad (4)$$

where I is charge/discharge current, Δt is the discharge time, ΔV is 1 V, and m is the mass of active material within the electrode. The variation of the specific capacitance of Mn_3O_4 samples with current density is given in Supporting information S4. The Mn_3O_4 stacked nanosheet electrodes have a good electrochemical reversibility and a large specific capacitance of 393 F g^{-1} (M1), 329 F g^{-1} (M2) and 274 F g^{-1} (M3) at a current density of 0.005 A cm^{-2} . The supercapacitance values obtained from CVs and charge–discharge studies are in very good agreement. The good capacitive behavior of Mn_3O_4 samples is a combined contribution of high porosity with superior pore-channel structure and large internal accessible surface which in turn facilitate the electrolyte penetration into the sample matrix, decrease the ion diffusion resistance and enhance the electro-active surface utilization during the redox process. Further, numerous nanochannels and higher pore volume of the sample act as “ion-buffering reservoirs” which reduce the mean

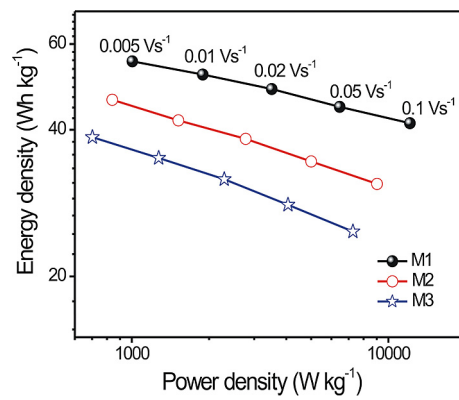


Fig. 9. The power density vs. energy density of stacked nanosheets of Mn_3O_4 samples in a Ragone plot.

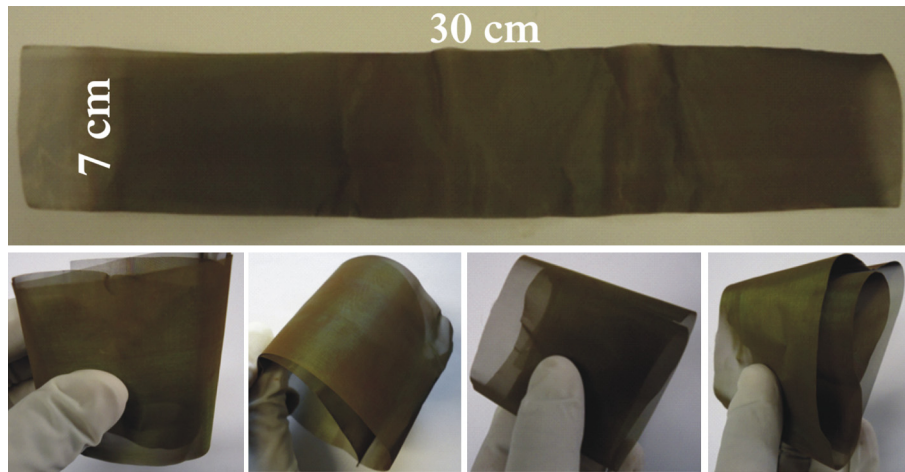


Fig. 10. Digital photographs of Mn_3O_4 stacked nanosheets on highly flexible mesh-like stainless steel substrate having area 210 cm^2 showing the feasibility of CBD method for large area deposition on virtually any kind of substrate.

free path of the anions and facilitate faster ionic and electronic kinetics, thus maximizing the reversible insertion/de-insertion reactions. Sample M3, due to lower surface area, pore volume and agglomerated thick nanosheet-like structure, contains lower number of electro-active surface sites, and the irregular pores as well as disoriented pore walls induce random scattering of H^+ and Na^+ ions, which enhance the diffusion resistance and decrease the kinetics of these ions inside the sample matrix.

Electrochemical impedance technique is used to measure the impedance of a system over a range of frequencies, including the energy storage and dissipation properties. Fig. 8a shows the Nyquist plots of all three samples (M1, M2 and M3) of stacked Mn_3O_4 nanosheets measured at open circuit potential. The plot can be divided into two regions in which the first is semicircle at high frequency region corresponding to faradic reactions (i.e., charge transfer resistance between electrode and electrolyte) and the second is a straight line at low frequency region for the diffusion controlled process in the electrolyte. Furthermore, the sharp spike in the plots indicates that the diffusion and adsorption of ions onto the electrode surface is very fast, which results in negligible Warburg impedance. The internal solution resistance R_s of $0.48 \Omega \text{ cm}^{-2}$ and the charge transfer resistance R_{ct} of 10.22 , 23.03 and $35.42 \Omega \text{ cm}^{-2}$ can be estimated for the samples M1, M2 and M3, respectively. From this observation, it is concluded that as the concentration of HMT increases the stacking of nanosheets becomes more compact, leading to increase in the charge transfer resistance. The resistance value obtained in the present study was lower than that in the previous report for Mn_3O_4 with rough morphology [41]. This is an advantage of stacked nanosheets-like morphology and the resulting porous space. It is interesting to note that the pores in the stacked nanosheets may improve the diffusivity of the electrolyte ions, reducing the series resistance at the Mn_3O_4 -electrolyte interface. The Fig. 8b shows the Bode plots of the samples. The values of power correspond to the heat production at the internal resistance and loss factors of electrode in the lower and higher frequency region are tabulated in Table 1. These results obtained from the Bode plot are similar to the effect of scan rate on supercapacitance where specific capacitance decreases with increase in scan rate. Therefore the value of specific capacitance obtained at lower scan rate is appropriate for good performance of electrode material [42].

The values of power density (PD) and energy density (ED) of Mn_3O_4 stacked nanosheets are calculated from the CV measurements at different scan rates from the equation [43,44]:

$$\text{ED} = CV^2/2 \quad (5)$$

where C is the specific capacitance (Fg^{-1}) at a particular potential scan rate and V is the potential window (here it is 1.0 V). The PD values of Mn_3O_4 nanosheets are calculated by dividing the respective ED values with time “ t ” for one cyclic sweep at the corresponding scan rate.

$$\text{PD} = \text{ED}/t \quad (6)$$

The graph of PD vs. ED values for all the three Mn_3O_4 samples (M1, M2 and M3) is plotted and compared with the standard Ragone plot [45] as shown in Fig. 9. From the graph, it is seen that all these Mn_3O_4 stacked nanosheet electrodes demonstrate relatively higher energy density than conventional capacitors and ultracapacitors and higher power density than the conventional batteries and fuel cells. These results proved that the stacked nanosheet-like Mn_3O_4 is a promising material for the fabrication electrodes in supercapacitor devices.

It is worth noting that the selective formation of stacked Mn_3O_4 nanosheets has also been achieved on large area ($30 \text{ cm} \times 7 \text{ cm} = 210 \text{ cm}^2$) of highly flexible stainless steel mesh-like substrate (Fig. 10), which proves that CBD is convenient for large area deposition (i.e., high mass production). In the recent years, we are in strong need of the lightweight, compact and mechanically flexible energy storage devices to improve the transportability of the energy for different applications [46]. Thus, the supercapacitors based on stacked Mn_3O_4 nanosheets onto flexible substrate are very promising in the field of lightweight, ultrathin energy management devices for wearable electronics [47].

4. Conclusions

In conclusion, a mild, simple and scalable chemical bath deposition method has been developed to synthesize thin films of stacked Mn_3O_4 nanosheets with different sizes and crystalline natures. This method may offer an elegant route for the direct growth of nanostructured Mn_3O_4 on different substrate surfaces. Also, it was proved that the method can be achieved convenient for large area deposition ($>200 \text{ cm}^2$), which opens up the opportunities for large mass production of electrode material. Based on these stacked nanostructures, the relationships between the specific area, crystallinity and the electrochemical performances have been discussed in our work. The results demonstrated that all of the

samples revealed enhanced electrochemical performances due to the relatively high utilization of the active materials. Among three samples, the sample synthesized at low concentration of hexamethylenetetramine, with an especially high specific area ($104 \text{ m}^2 \text{ g}^{-1}$), uniform pore size distribution and poor crystallinity, demonstrated the highest specific capacitance with a high rate and cycling stability. It is thought that the porous stacked nanostructures can serve as promising electrode materials for high-performance flexible supercapacitors.

Acknowledgment

One of the authors (D.P.D.) appreciates the award of a Humboldt Fellowship of the Alexander von Humboldt Foundation (AvH), Germany. Authors are also thankful to Mr. Torsten Jagemann and Dr. Steffen Schulze from Physics Department, Chemnitz University of Technology for SEM and TEM measurements.

Appendix A. Supplementary data

Supplementary data related to this article can be found at <http://dx.doi.org/10.1016/j.jpowsour.2013.01.198>.

References

- [1] H.B. Zeng, X.J. Xu, Y. Bando, U.K. Gautam, T.Y. Zhai, X.S. Fang, B.D. Liu, D. Golberg, *Adv. Funct. Mater.* 19 (2009) 3165–3172.
- [2] Y. Yin, A.P. Alivisatos, *Nature* 437 (2005) 664–670.
- [3] A.S. Arico, P. Bruce, B. Scrosati, J.M. Tarascon, W.V. Schalkwijk, *Nat. Mater.* 4 (2005) 366–377.
- [4] C. Burda, X.B. Chen, R. Narayanan, M.A. El-Sayed, *Chem. Rev.* 105 (2005) 1025–1102.
- [5] D.P. Dubal, S.H. Lee, J.G. Kim, W.B. Kim, C.D. Lokhande, *J. Mater. Chem.* 22 (2012) 3044–3052.
- [6] M. Kaempgen, C.K. Chan, J. Ma, Y. Cui, G. Gruner, *Nano Lett.* 9 (2009) 1872–1876.
- [7] C.D. Lokhande, D.P. Dubal, O.S. Joo, *Curr. Appl. Phys.* 11 (2011) 255–270.
- [8] L.T. Lam, R. Louey, *J. Power Sources* 158 (2006) 1140–1148.
- [9] M. Winter, R.J. Brodd, *Chem. Rev.* 104 (2004) 4245–4269.
- [10] D.P. Dubal, A.D. Jagadale, C.D. Lokhande, *Electrochim. Acta* 80 (2012) 160–170.
- [11] Y.F. Lee, K.H. Chang, C.C. Hu, Y.H. Chu, *J. Power Sources* 206 (2012) 469–475.
- [12] M.S. Wu, R.H. Lee, *J. Power Sources* 176 (2008) 363–368.
- [13] Q.T. Qu, P. Zhang, B. Wang, Y.H. Chen, S. Tian, Y.P. Wu, R. Holze, *J. Phys. Chem. C* 113 (2009) 14020–14027.
- [14] L. Ji, A. Medford, X. Zhang, *J. Mater. Chem.* 19 (2009) 5593–5601.
- [15] T. Zhou, S. Mo, S. Zhou, W. Zou, Y. Liu, D. Yuan, *J. Mater. Sci.* 46 (2011) 3337–3342.
- [16] D.R. Rolison, *Science* 299 (2003) 1698–1701.
- [17] J.W. Long, B. Dunn, D.R. Rolison, H.S. White, *Chem. Rev.* 104 (2004) 4463–4492.
- [18] K. Yang, G. She, H. Wang, X. Ou, X. Zhang, C. Lee, S. Lee, *J. Phys. Chem. C* 113 (2009) 20169–20172.
- [19] T. Ghoshal, S. Biswas, P.M.G. Nambissan, G. Majumdar, S.K. De, *Cryst. Growth Des.* 9 (2009) 1287–1292.
- [20] P. Li, C.Y. Nan, Z. Wei, J. Lu, Q. Peng, Y.D. Li, *Chem. Mater.* 22 (2010) 4232–4236.
- [21] M. Fang, X.L. Tan, M. Liu, S.H. Kang, X.Y. Hu, L.D. Zhang, *Cryst. Eng. Commun.* 13 (2011) 4915–4920.
- [22] D.P. Dubal, V.J. Fulari, C.D. Lokhande, *Microporous Mesoporous Mater.* 51 (2012) 511–516.
- [23] X. Gao, X. Li, W. Yu, *J. Phys. Chem. B* 109 (2005) 1155–1161.
- [24] M. Salavati-Niasari, F. Davar, M. Mazaheri, *Polyhedron* 27 (2008) 3467–3471.
- [25] D.P. Dubal, R. Holze, *RSC Adv.* 2 (2012) 12096–12100.
- [26] H.Y. Xu, S.L. Xu, X.D. Li, H. Wang, H. Yan, *Appl. Surf. Sci.* 252 (2006) 4091–4096.
- [27] L.E. Greene, B.D. Yuhas, M. Law, D. Zitoun, P.D. Yang, *Inorg. Chem.* 45 (2006) 7535–7543.
- [28] C.Z. Yuan, X.G. Zhang, L.H. Su, B. Gao, L.F. Shen, *J. Mater. Chem.* 19 (2009) 5772–5777.
- [29] F. Chen, R.J. Zhou, L.G. Yang, N. Liu, M. Wang, H.Z. Chen, *J. Phys. Chem. C* 112 (2008) 1001–1007.
- [30] L.X. Yang, Y.J. Zhu, H. Tong, Z.H. Liang, W.W. Wang, *Cryst. Growth Des.* 7 (2007) 2716–2719.
- [31] P.S. Shah, J.D. Holmes, K.P. Johnston, B.A. Korgel, *J. Phys. Chem.* 106 (2002) 2545–2551.
- [32] R.J. Iwanowski, M.H. Heinonen, E. Janik, *Chem. Phys. Lett.* 387 (2004) 110–115.
- [33] Z.P. Feng, G.R. Li, J.H. Zhong, Z.L. Wang, Y.N. Ou, Y.X. Tong, *Electrochem. Commun.* 11 (2009) 706–710.
- [34] M.W. Xu, L.B. Kong, W.J. Zhou, H.L. Li, *J. Phys. Chem. C* 111 (2007) 19141–19147.
- [35] T. Xue, C.L. Xua, D.D. Zhao, X.H. Li, H.L. Li, *J. Power Sources* 164 (2007) 953–958.
- [36] Y. Dai, K. Wang, J.Y. Xie, *Appl. Phys. Lett.* 90 (2007) 104102–104104.
- [37] K.A.M. Ahmed, Q.M. Zeng, K.B. Wu, K.X. Huang, *J. Solid State Chem.* 183 (2010) 744–751.
- [38] D.P. Dubal, D.S. Dhawale, R.R. Salunkhe, V.J. Fulari, C.D. Lokhande, *J. Alloys Compd.* 497 (2010) 166–170.
- [39] P.M. Kulal, D.P. Dubal, C.D. Lokhande, V.J. Fulari, *J. Alloys Compd.* 509 (2011) 2567–2571.
- [40] W. Sugimoto, H. Iwata, Y. Yasunaga, Y. Murakami, Y. Takasu, *Angew. Chem. Int. Ed.* 42 (2003) 4092–4096.
- [41] D.P. Dubal, D.S. Dhawale, R.R. Salunkhe, C.D. Lokhande, *J. Electrochem. Soc.* 157 (2010) A812–A817.
- [42] P.R. Deshmukh, S.N. Pusawale, V.S. Jamadade, C.D. Lokhande, *J. Alloys Compd.* 509 (2011) 5064–5069.
- [43] J. Li, F. Gao, *J. Power Sources* 194 (2009) 1184–1193.
- [44] D.P. Dubal, G.S. Gund, C.D. Lokhande, R. Holze, *Mater. Res. Bull.* 48 (2013) 923–928.
- [45] B.C. Jones, A.F. Hollenkamp, S.W. Donne, *J. Electrochem. Soc.* 157 (2010) A551–A557.
- [46] K. Fic, G. Lota, M. Meller, E. Frackowiak, *Energy Environ. Sci.* 5 (2012) 5842–5850.
- [47] L.B. Hu, M. Pasta, F. La Mantia, L.F. Cui, S. Jeong, H.D. Deshazer, J.W. Choi, S.M. Han, Y. Cui, *Nano Lett.* 10 (2010) 708–714.